GEOPHYSICS, VOL. 78, NO. 5 (SEPTEMBER-OCTOBER 2013); P. WC51–WC63, 22 FIGS.
10.1190/GEO2012-0394.1

Multiparameter TTI tomography of P-wave reflection and VSP data

Xiaoxiang Wang[1] and Ilya Tsvankin[2]

ABSTRACT

Transversely isotropic models with a tilted symmetry axis (TTI media) are widely used in depth imaging of complex geologic structures. Here, we present a modification of a previously developed 2D P-wave tomographic algorithm for estimating heterogeneous TTI velocity fields and apply it to synthetic and field data. The symmetry-direction velocity V_{P0}, anisotropy parameters ε and δ, and symmetry-axis tilt ν are defined on a rectangular grid. To ensure stable reconstruction of the TTI parameters, reflection data are combined with walkaway vertical seismic profiling (VSP) traveltimes in joint tomographic inversion. To improve the convergence of the algorithm, we develop a three-stage model-updating procedure that gradually relaxes the constraints on the spatial variations of the anisotropy parameters, while the symmetry axis is kept orthogonal to the reflectors. Only at the final stage of the inversion are the parameters V_{P0}, ε, and δ updated on the same grid. We also incorporate geologic constraints into tomography by designing regularization terms that penalize parameter variations in the direction parallel to the interfaces. First, we examine the performance of the regularized joint tomography of reflection and VSP data for two sections of the BP TTI model that contain an anticline and a salt dome. All three TTI parameters in the shallow part of both sections (down to 5 km) are well resolved by the proposed model-updating process. Then, the algorithm is applied to a 2D section from 3D ocean-bottom seismic data acquired at Volve field in the North Sea. The inverted TTI model produces well-focused reflectors throughout the section and accurately positions the key horizons, which is confirmed by the available well markers.

INTRODUCTION

Prestack depth imaging for complex geologic environments (including subsalt plays and fold-and-thrust belts) requires anisotropic velocity models such as transverse isotropy with a vertical (VTI) or tilted (TTI) axis of symmetry. A stable velocity-analysis tool for prestack migration is reflection tomography in the migrated domain (Stork, 1992), which has been extended to heterogeneous TI media (Campbell et al., 2006; Woodward et al., 2008). A review of published migration velocity analysis (MVA) algorithms for TTI media can be found in our previous paper (Wang and Tsvankin, 2013).

P-wave kinematics in TTI media are controlled by the velocity V_{P0} in the symmetry-axis direction, anisotropy parameters ε and δ, and the orientation of the symmetry axis (in 2D defined by the tilt ν from the vertical). To ensure the stability of inversion, the symmetry-axis orientation is commonly assumed to be known from structural information. For example, the symmetry axis can be taken perpendicular to the reflector, which is usually the case for dipping shale layers. Then in 2D, the tilt is equal to the reflector dip, which can be estimated from the depth image.

Most current parameter-estimation techniques either rely on relatively simple model representation (e.g., layer- or block-based models used by Behera and Tsvankin [2009]) or simplify the inversion by keeping the anisotropy parameters ε and δ fixed and updating only the symmetry-direction velocity V_{P0} on a grid (Charles et al., 2008; Huang et al., 2008). However, restricting updates to just V_{P0} does not adequately describe anisotropic velocity fields and makes it difficult to fit the normal-moveout (NMO) velocities for horizontal and dipping events. Zhou et al. (2011) demonstrate

Manuscript received by the Editor 23 September 2012; revised manuscript received 17 April 2013; published online 11 September 2013; corrected version published online 17 September 2013.
[1]Formerly Colorado School of Mines, Center for Wave Phenomena, Geophysics Department, Golden, Colorado, USA; presently Shell Exploration and Production Company, New Orleans, Louisiana, USA. E-mail: xiaoxiang.wang@shell.com.
[2]Colorado School of Mines, Center for Wave Phenomena, Geophysics Department, Golden, Colorado, USA. E-mail: ilya@dix.mines.edu.

that simultaneous estimation of all three relevant parameters (V_{P0}, ε, and δ) provides a better approximation to the data than single-parameter inversion. Because P-wave reflection traveltimes typically cannot constrain all relevant TTI parameters, additional information is required to reduce the nonuniqueness of the inverse problem (Morice et al., 2004; Tsvankin, 2005; Bakulin et al., 2010b). However, there are few publications on such joint inversion of P-wave reflections and other data (e.g., VSP traveltimes) for anisotropic media.

Nonuniqueness of the inversion of reflection data can also be mitigated by regularization, which imposes a priori constraints on the estimated model (Engl et al., 1996). Wang and Tsvankin (2013) use Tikhonov (1963) regularization to smooth the velocity field with equal weights in the horizontal and vertical directions. Fomel (2007) develops so-called shaping regularization designed to steer velocity variations along geologic structures (e.g., layers). His mapping (shaping) operator is integrated into a conjugate-gradient iterative solver. Using the steering-filter preconditioner (Clapp et al., 2004) similar to shaping regularization, Bakulin et al. (2010c) perform joint tomographic inversion of horizontal and dipping P-wave reflection events and check-shot traveltimes for VTI media. They conclude that in the vicinity of the well it is possible to resolve the vertical variation of all three relevant parameters (V_{P0}, ε, and δ). In a case study, Bakulin et al. (2010a) compare several techniques for building VTI and TTI models using borehole-calibrated profiles of the anisotropy parameters. They find that the velocity field obtained by interpolation that conforms to several key horizons produces the smallest well misties and minimizes residual moveout in common-image gathers (CIGs).

Wang and Tsvankin (2013) develop a 2D ray-based tomographic algorithm for iteratively updating the parameters V_{P0}, ε, and δ of TTI media defined on rectangular grids (the symmetry axis is set orthogonal to the imaged reflectors). Synthetic tests for models with a quasi-factorized TTI syncline (i.e., ε and δ are constant inside the TTI layer, whereas the tilt ν may vary spatially) and a TTI thrust sheet demonstrate that stable parameter estimation requires strong smoothness constraints or additional information from walkaway VSP traveltimes.

Here, we first introduce the objective function that includes the residual moveout in CIGs and the VSP traveltime misfit supplemented by regularization terms. The regularization is designed to smooth the parameters in the direction parallel to the interfaces, while allowing for more pronounced variations in the orthogonal direction. Next, we present a three-stage inversion methodology in which gridded tomography is preceded by two partial parameter-updating steps designed to stabilize the inversion. Then the tomographic algorithm is tested on two sections of the 2D TTI model devised by BP and a line from 3D ocean bottom seismic (OBS) data provided by Statoil.

METHODOLOGY

Basic elements of the tomographic algorithm used here are described in Wang and Tsvankin (2013). The residual moveout in CIGs produced by prestack Kirchhoff depth migration is minimized during iterative parameter updates. If walkaway VSP surveys (check shots represent zero-offset VSP data) are available, VSP traveltimes are computed for each trial model and included in the following objective function F:

$$F(\Delta\boldsymbol{\lambda}) = \left\|\mathbf{A}\Delta\boldsymbol{\lambda} - \mathbf{b}\right\|^2 + \zeta_{\mathrm{VSP}}^2\left\|\mathbf{E}\Delta\boldsymbol{\lambda} - \mathbf{d}\right\|^2 + R(\Delta\boldsymbol{\lambda}), \quad (1)$$

where $\Delta\boldsymbol{\lambda}$ is a vector composed of the parameter updates (ΔV_{P0}, $\Delta\varepsilon$, and $\Delta\delta$) at each grid point, the elements of the matrix $\mathbf{A}$ are the traveltime derivatives with respect to the medium parameters at each grid point ($\mathbf{A}$ is computed analytically along the raypaths), $\mathbf{b}$ is a vector containing the residual moveout in CIGs, the matrix $\mathbf{E}$ includes VSP traveltime derivatives, and the vector $\mathbf{d}$ is the difference between the observed and calculated VSP traveltimes for each source-receiver pair. The regularization term R in equation 1 has the form:

$$R(\Delta\boldsymbol{\lambda}) = \zeta^2\left\|\Delta\boldsymbol{\lambda}\right\|^2 + \zeta_1^2\left\|\mathbf{L}_1(\Delta\boldsymbol{\lambda} + \boldsymbol{\lambda}^0)\right\|^2 + \zeta_2^2\left\|\mathbf{L}_2(\Delta\boldsymbol{\lambda} + \boldsymbol{\lambda}^0)\right\|^2, \quad (2)$$

where $\zeta^2\left\|\Delta\boldsymbol{\lambda}\right\|^2$ restricts the magnitudes of parameter updates that have small derivatives in matrices $\mathbf{A}$ and $\mathbf{E}$, $\boldsymbol{\lambda}^0$ is the vector of model parameters obtained in the previous iteration, the operators $\mathbf{L}_1$ and $\mathbf{L}_2$ are designed to make parameter variations more pronounced in the direction normal to the interfaces, and ζ, ζ_1, and ζ_2 are the regularization coefficients/weights. The choice of the weighting coefficients depends on several factors, such as the data volume, number of grid points, and desired smoothness of the model. In 2D, the normal direction of a reflector is defined by the dip angle with the vertical, which is computed from the depth image using Madagascar program "sfdip." Then, the symmetry-axis tilt ν at each grid point is set equal to the corresponding dip.

To construct the matrix $\mathbf{L}_1$, we first compute two components of the gradient $\nabla\lambda$ from a finite-difference approximation:

$$\lambda'(x) = \frac{\lambda(x + \mathrm{d}x) - \lambda(x - \mathrm{d}x)}{2\,\mathrm{d}x} + O[(\mathrm{d}x)^2], \quad (3)$$

$$\lambda'(z) = \frac{\lambda(z + \mathrm{d}z) - \lambda(z - \mathrm{d}z)}{2\,\mathrm{d}z} + O[(\mathrm{d}z)^2], \quad (4)$$

where λ is the parameter (V_{P0}, ε, or δ) at the grid point with the coordinates x and z, and $\mathrm{d}x$ and $\mathrm{d}z$ are the cell dimensions. Because the dip field yields the vector $\mathbf{n}$ orthogonal to reflectors, we minimize the norm of the cross product $\|\mathbf{n}\times\nabla\lambda\|$ at all grid points, which is equivalent to aligning the direction of the largest parameter variation with $\mathbf{n}$ and restricting the variations along the interfaces. More cells can be included by using a higher order finite-difference approximation:

$$\lambda'(x) = [-\lambda(x + 2\mathrm{d}x) + 8\lambda(x + \mathrm{d}x) - 8\lambda(x - \mathrm{d}x) + \lambda(x - 2\mathrm{d}x)]/(12\mathrm{d}x) + O[(\mathrm{d}x)^4], \quad (5)$$

$$\lambda'(z) = [-\lambda(z + 2\mathrm{d}z) + 8\lambda(z + \mathrm{d}z) - 8\lambda(z - \mathrm{d}z) + \lambda(z - 2\mathrm{d}z)]/(12\mathrm{d}z) + O[(\mathrm{d}z)^4]. \quad (6)$$

Similarly, the operator $\mathbf{L}_2$ is built from the cross product of $\mathbf{n}$ and the following two-component vector formed by second-order derivatives:

$$\lambda''(x) = \frac{\lambda(x+\mathrm{d}x) - 2\lambda(x) + \lambda(x-\mathrm{d}x)}{(\mathrm{d}x)^2}, \quad (7)$$

$$\lambda''(z) = \frac{\lambda(z+\mathrm{d}z) - 2\lambda(z) + \lambda(z-\mathrm{d}z)}{(\mathrm{d}z)^2}. \quad (8)$$

Then we minimize the norm of the cross-product to smooth the parameter variations in the direction parallel to the interfaces.

Defining the TTI parameters on a relatively small grid results in a large number of unknowns, and the Fréchet matrices **A** and **E** in equation 1 are sparse (i.e., only nonzero or relatively large elements are stored due to the limited computer memory). To solve such a large sparse linear system of equations in an efficient way, we use a parallel direct sparse solver (PARDISO, Naumann and Schenk, 2011).

The anisotropic velocity field is iteratively updated starting from an initial model that may be obtained from stacking-velocity tomography at borehole locations (Wang and Tsvankin, 2010). In the first few iterations, the symmetry-direction velocity V_{P0} is typically inaccurate, and simultaneous inversion for all TTI parameters may result in unacceptably large updates for ε and δ. If the anisotropy parameters are moderate (in the test below, ε<0.25 and δ<0.15), it is convenient to fix them temporarily at the initial values (typically small) and limit the updates to the gridded velocity V_{P0}. When iterations no longer significantly reduce the data misfit, we move on to the second stage of parameter updating. At that stage, the model is divided into several layers based on the picked reflectors, and the anisotropy parameters are assumed to be spatially invariant within each layer. The velocity V_{P0} is then updated on a grid, whereas the inversion for ε and δ is layer-based. Such a quasi-factorized assumption is equivalent to strong smoothing of ε and δ and may help resolve all TTI parameters if V_{P0} is a linear function of the spatial coordinates and at least two distinct dips are available (Behera and Tsvankin, 2009). At the third and last stage of velocity analysis, the anisotropy parameters are updated on the same grid as that for V_{P0} to allow for more realistic treatment of heterogeneity. Still, because P-wave kinematics are less sensitive to anisotropy than to the symmetry-direction velocity, the ε- and δ-fields in equation 2 are typically regularized with larger weights.

BP ANTICLINE MODEL

First, we test the joint tomography of P-wave long-spread reflection data and walkaway VSP traveltimes on a section of the TTI model produced by BP. That section contains an anticline structure surrounded by gently dipping anisotropic layers. The velocity V_{P0} in the actual model is smoothly varying (Figure 1a), except for a small jump at the water bottom. The symmetry axis is set perpendicular to the interfaces (Figure 1b), and the anisotropy parameters ε and δ change from layer to layer. Note that the lateral variations of ε and δ are relatively weak compared with those of V_{P0} (Figure 1c and 1d). The depth image produced by Kirchhoff prestack depth migration with the actual velocity model is shown in Figure 2.

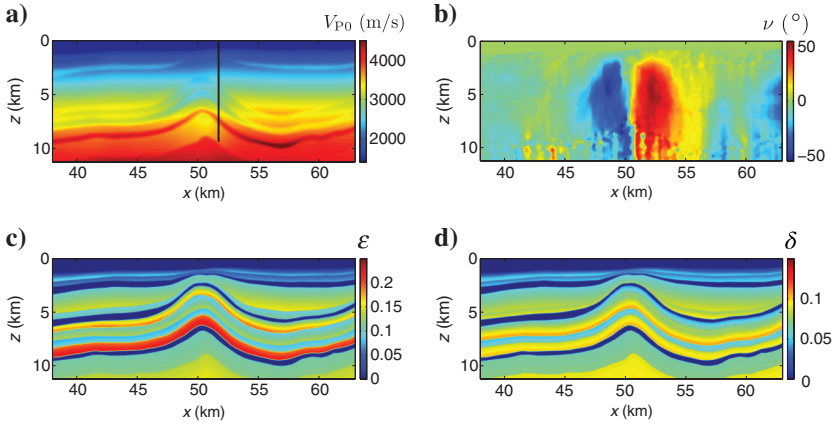

Figure 1. Section of the BP TTI model that includes an anticline (the grid size is 6.25 × 6.25 m). The top water layer is isotropic with velocity 1492 m/s. (a) The symmetry-direction velocity V_{P0}. The black line marks a vertical "well" at $x = 51.4$ km. (b) The symmetry-axis tilt ν. The anisotropy parameters (c) ε and (d) δ.

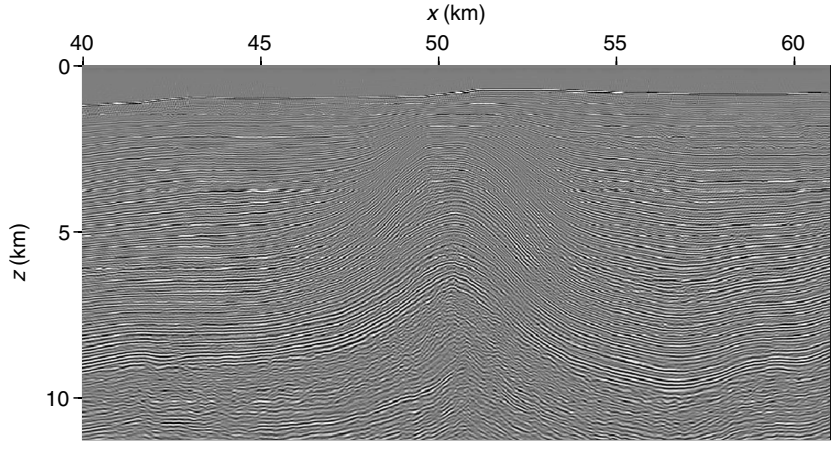

Figure 2. Depth image of the BP anticline model produced with the actual parameters from Figure 1.

The tomographic algorithm is applied to CIGs from $x = 40$ to 61 km with an interval of 150 m (the maximum offset is 10 km). Synthetic VSP data were generated by BP in a vertical well placed at location $x_{\mathrm{VSP}} = 51.4$ km with 24 receivers spanning the interval of depth from $z = 4756.25$ to 5043.75 m every 12.5 m and 24 more receivers evenly placed between 7837.5 and 8125 m. The VSP sources were located at the surface every 50 m from $x = 41.4$ to 61.4 km (the maximum offset is also 10 km). In addition, check-shot traveltimes were recorded every 50 m from $z = 943.5$ to 9493.75 m.

To build an initial model, we compute a 1D profile of V_{P0} from the check-shot traveltimes and then obtain the 2D velocity field (Figure 3a) by extrapolation that conforms to the picked interfaces. Clearly, the errors in V_{P0} are expected to increase away from the well. The initial model is isotropic, with ε and δ set to zero. The exact position of the water bottom is assumed to be known, and the velocity of the water layer is fixed at the correct value. The noticeable residual moveout in the CIGs (Figure 3b) indicates that the velocity field contains significant errors.

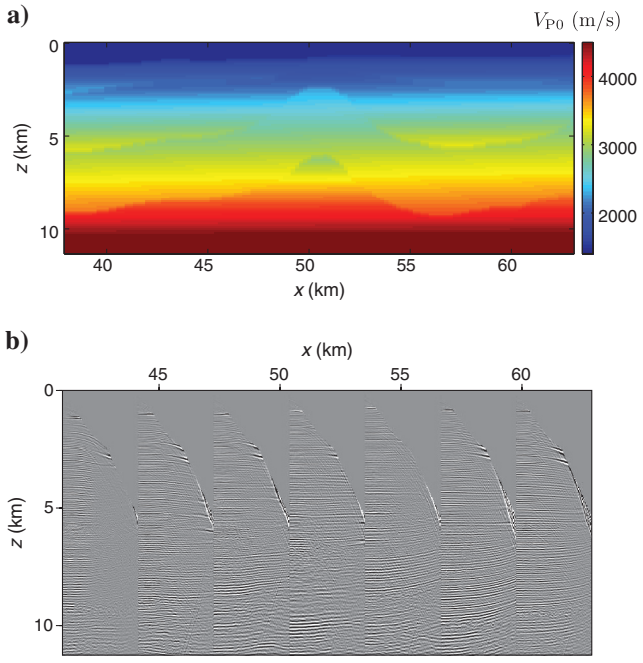

Figure 3. (a) Initial isotropic model with the velocity V_{P0} defined on a 200×100 m grid. The velocity in the water is set to the correct value. (b) CIGs (displayed every 3 km from 41 to 62 km) computed with the initial model from Figure 3a.

Velocity analysis is performed using the three-stage parameter-estimation procedure described above, which operates with reflection and VSP data. First, we update only the velocity V_{P0} defined on a rectangular 200×100 m grid, while keeping the model isotropic (i.e., $\varepsilon = \delta = 0$). Then, ε and δ are taken constant in each layer (delineated by the interfaces picked on the image from the previous iteration) and updated simultaneously with V_{P0}. Because the anisotropy parameters in thin (compared with their depth) intervals cannot be constrained just by reflection traveltimes, the model has to be divided into relatively coarse layers to ensure convergence of the inversion algorithm. With this quasi-factorized TTI assumption, the inverted model (Figure 4) reduces the residual moveout in CIGs (Figure 5) and the VSP traveltime misfit.

However, the residual moveout in Figure 5 is not completely removed, mainly because the assumption about the anisotropy parameters does not conform to the actual ε- and δ-fields (Figure 1c and 1d). To allow for more realistic spatial variations, at the last stage of parameter updating we estimate the parameters ε and δ on the same grid as the one used for the velocity V_{P0}. However, because the trade-offs between the parameters may cause large errors in ε and δ defined on fine grids, the anisotropy parameters should be

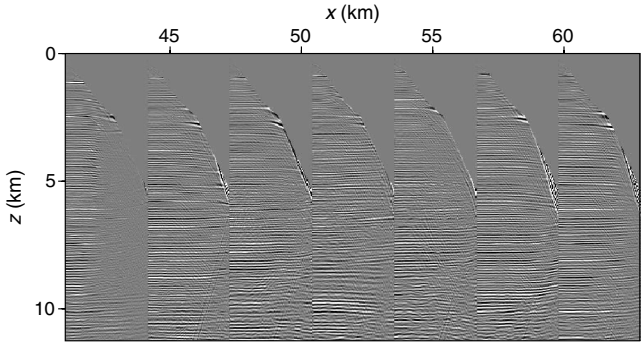

Figure 5. (a) CIGs obtained with the quasi-factorized TTI model from Figure 4.

Figure 4. Anticline model from Figure 1 updated using the quasi-factorized TTI assumption. (a) The symmetry-direction velocity V_{P0} estimated on a 200×100 m grid. (b) The tilt ν obtained by setting the symmetry axis perpendicular to the reflectors. The inverted interval parameters (c) ε and (d) δ, which are kept constant within each layer.

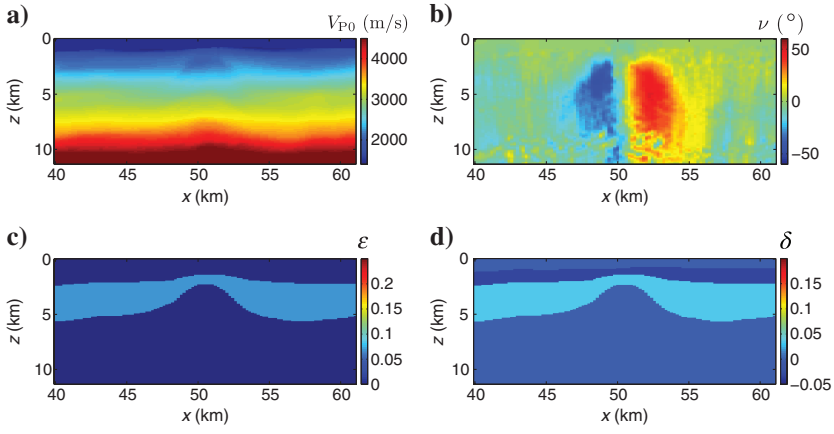

more tightly constrained, so the corresponding regularization coefficients are larger than those for V_{P0}.

After application of the joint tomography, the velocity V_{P0} above the depth $z = 7$ km is relatively well recovered with errors in most areas smaller than 4% (Figure 6a). The spatial variations of ε and δ are partially resolved from the water bottom down to $z = 5$ km (Figure 6c and 6d). The coverage of VSP rays, however, becomes more sparse with depth. Also, the offset-to-depth ratio of P-wave reflections is insufficient to constrain the parameter ε below 7 km, although the maximum offset reaches 10 km. Therefore, the accuracy in ε and δ decreases in the deep part of the section. Still, the final inverted model (Figure 6) almost eliminates the residual moveout in the CIGs (Figure 7a, except for locations close to the left and right edges due to poor ray coverage), and the reflections are well focused (Figure 7b), especially those above $z = 7$ km. Comparison with several interfaces imaged using the actual model (Figure 2) shows that the reflectors are accurately positioned in depth, with the misties smaller than 40 m near the well.

The total data misfit computed using equation 1 has been minimized after the final iteration of tomography. Still, because of the

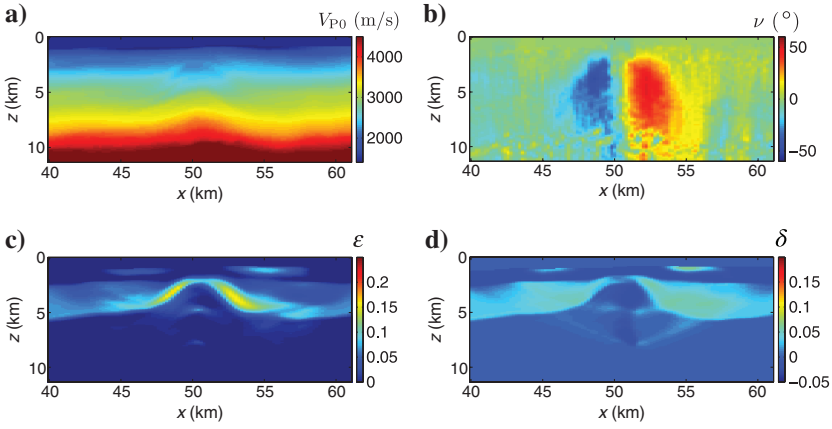

Figure 6. Inverted TTI parameters (a) V_{P0} (c) ε, and (d) δ after the final iteration of tomography. (b) The symmetry-axis tilt ν computed from the depth image obtained before the final iteration. The parameters V_{P0}, ε, and δ are estimated on a 200×100 m grid.

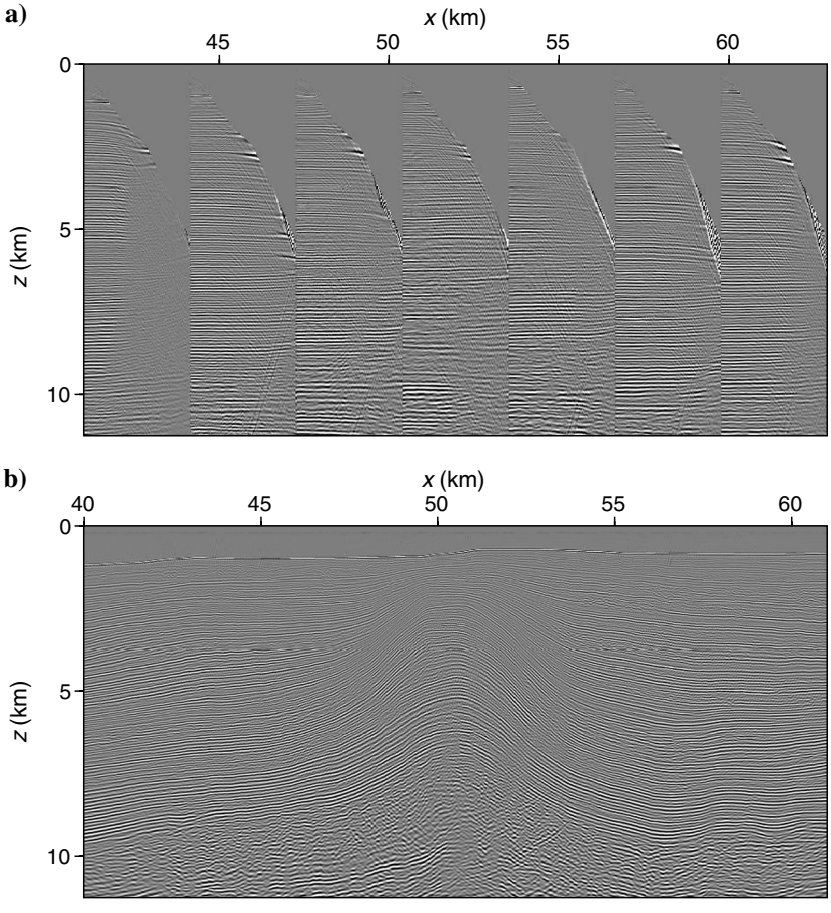

Figure 7. (a) CIGs and (b) the migrated section computed with the final inverted model from Figure 6.

trade-off between flattening the CIGs and minimizing the VSP traveltime misfit, the residual moveout could not be completely removed. Another reason for the remaining residual moveout is that the grid size may be too large to adequately represent the spatial parameter variations. The tomographic algorithm can only reconstruct a smooth approximation of the actual model.

An important parameter that influences the accuracy of the reconstructed velocity model is the symmetry-axis tilt ν, which is computed directly from the depth image. Poorly constrained TTI parameters in the deep part of the model yield a distorted image, which produces large errors in the estimated values of ν. The obtained tilt field is used for the next iteration of tomography, which further distorts the other estimated TTI parameters. Therefore, without sufficient constraints from deep reflection events and VSP rays, the trade-offs between the tilt ν and the other TTI parameters increase the uncertainty in velocity analysis at depth.

BP SALT MODEL

Next, the joint tomography is applied to another section of the BP TTI model that includes a salt dome (Figure 8). The top of the salt and the flanks right beneath it produce strong reflections and are clearly imaged by Kirchhoff depth migration, but the deeper segments of the flanks are blurred even when the actual model is used (Figure 9). The image quality can be improved with a wavefield-based imaging algorithm, such as reverse time migration.

The maximum offset (10 km) and the source and receiver intervals (50 m) are the same as in the previous test. The CIGs used for MVA are computed every 150 m from $x = 16$ to 46 km. The BP data set contains a vertical well at location $x_{\mathrm{VSP}} = 29.9$ km to the left of the salt body (Figure 8a). Two sets of evenly spaced 24 receivers (one between the depths $z = 5275$ and 5562.5 m and the other between $z = 8400$ and 8687.5 m) were placed in the well to record a walkaway VSP survey. The maximum offset for the VSP data is 10 km with a source interval of 50 m. The input data also include check-shot traveltimes obtained every 50 m from $z = 1743.75$ to 9093.75 m.

During the inversion, the water layer and salt body are kept isotropic with the velocities fixed at the actual values. Also, the positions of the top and flanks of the salt dome are assumed to be known, and the update is performed only for the sedimentary formations around the salt body. Because ray tracing becomes unstable in the presence of sharp velocity contrasts, we apply 2D smoothing to the velocity model to find the raypaths crossing the salt and then calculate the traveltimes and their derivatives in the original (unsmoothed) model.

Similar to the previous test, an initial isotropic model (Figure 10a) is built using check-shot traveltimes and extrapolation along interfaces. Because the symmetry-direction velocity (and other

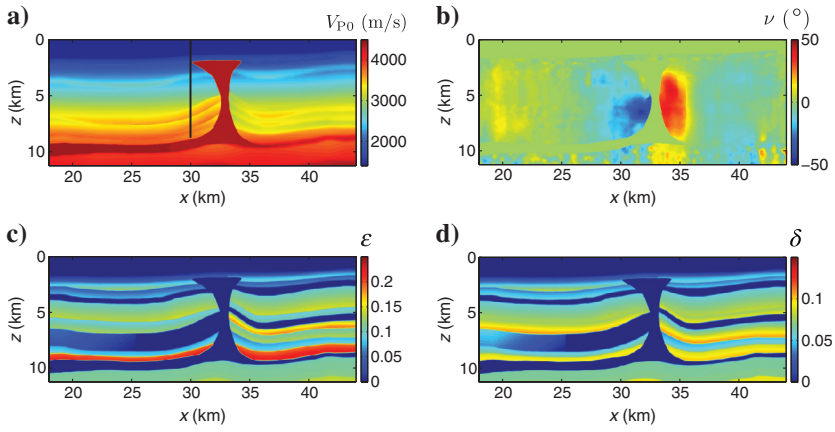

Figure 8. Section of the BP TTI model with a salt dome (the grid size is 6.25×6.25 m). The top water layer and the salt body are isotropic with the P-wave velocity equal to 1492 and 4350 m/s, respectively. (a) The symmetry-direction velocity V_{P0}. The vertical well at $x = 29.9$ km is marked by a black line. (b) The tilt of the symmetry axis, which is set orthogonal to the interfaces. The anisotropy parameters (c) ε and (d) δ.

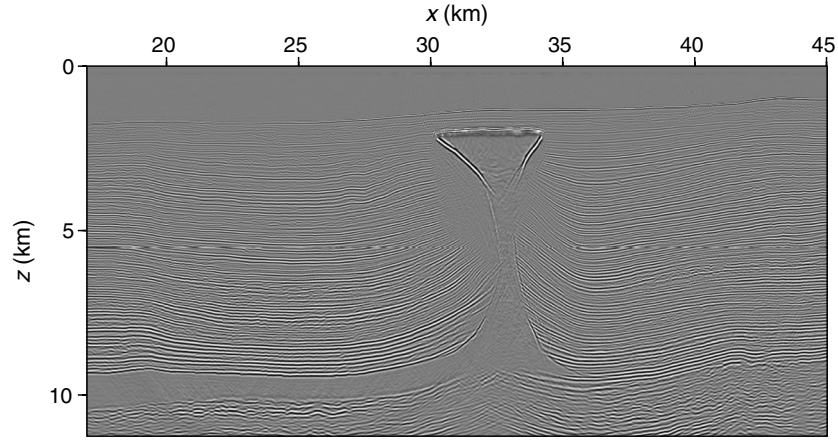

Figure 9. Depth image of the BP salt model produced with the actual parameters from Figure 8.

parameters) is different on the two sides of the salt body, the residual moveout in the CIGs (Figure 10b) is larger to the right of the salt (i.e., further away from the well).

As in the first test, the joint tomography is performed using the three-stage parameter-estimation procedure. For the VSP sources to the left of the well, the corresponding rays pass through the relatively simple sedimentary section. The VSP rays originated to the right of the well, however, cross the high velocity salt body, and errors in the velocity field near the salt boundaries may cause large perturbations of the ray trajectories. Therefore, we assign smaller weights in the objective function to the VSP traveltimes for the sources located to the right of the well. As a result, the anisotropic velocity field on the right side of the salt dome has to be determined mostly from the P-wave reflection data, which leads to larger uncertainty in the TTI parameters.

After all three parameters were updated on the same grid at the last stage of the updating procedure, the velocity V_{P0} (Figure 11a) above the depth $z = 7$ km to the left of the salt body is relatively well resolved (errors in most areas do not exceed 3%). However, the errors in V_{P0} on the right side of the section are higher because of the limited constraints from VSP data, as described above. The spatial variations of ε and δ are partially recovered from the water bottom down to $z = 5$ km (Figure 11c and 11d). Because of the smaller offset-to-depth ratio and poor coverage of VSP rays (especially for

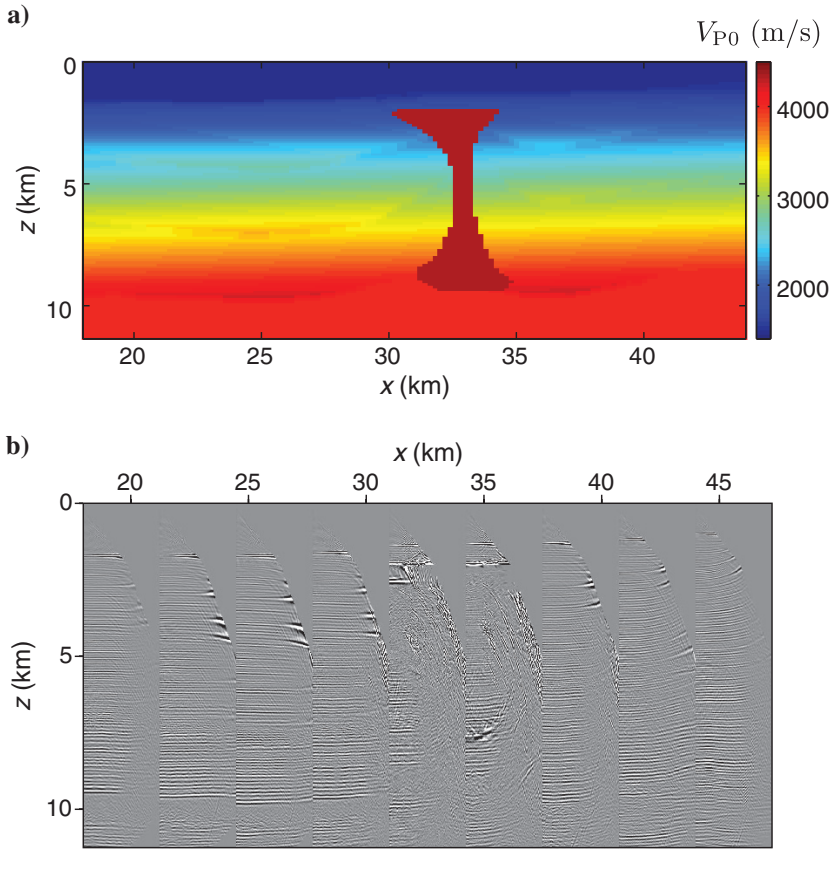

Figure 10. (a) Initial isotropic model with V_{P0} defined on a 200×100 m grid. The P-wave velocities in the top water layer and salt body are set to the actual values. (b) CIGs (displayed every 3.25 km from 18 to 44 km) computed with the initial model from Figure 10a.

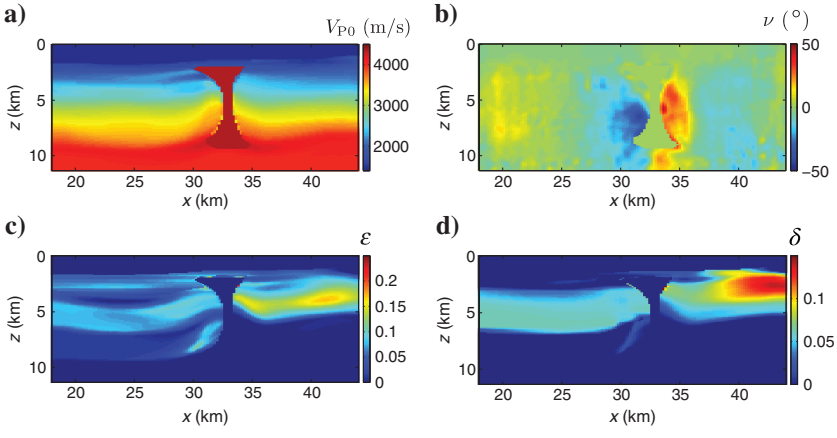

Figure 11. Inverted TTI parameters (a) V_{P0}, (c) ε, and (d) δ after the final iteration of joint tomography. (b) The symmetry-axis tilt ν computed from the depth image obtained before the final iteration. The parameters V_{P0}, ε, and δ are estimated on a 200×100 m grid.

the right part of the model) at depth, the anisotropy parameters for most grid points below 5 km could not be updated.

Despite these problems, the final model flattens most CIGs (Figure 12a) and practically eliminates the VSP traveltime misfit. As a result, the migrated image (Figure 12b) reproduces the actual section with sufficient accuracy, except for the steep segments of the salt boundaries.

VOLVE OBS DATA

Volve field is located offshore Norway in the gas/condensate-rich Sleipner area of the North Sea (Figure 13a). It is a small oil field with a dome-shaped structure formed by the collapse of adjacent salt ridges during the Jurassic period (Szydlik et al., 2007). The reservoir in the Middle Jurassic Hugin sandstone formation is a structural trap bounded by faults which are mainly associated with salt tectonics (Figure 13b).

In 2002, a 3D OBS survey was acquired over a 12.3×6.8 km area of the field (Figure 14). Six swaths of 4C data were recorded using inline shooting geometry. Each swath includes two 6 km-long cables placed on the seafloor (about 92 m below the water surface) with 400-m spacing (Figure 14), and a cable contains 240 receivers with an interval of 25 m. In each swath, flip-flop shooting was conducted along 25 dual-source sail lines with 100 m separation. The sail line is 12 km long with a shot interval of 25 m (50 m between the flips).

The acquired 3D PP and PS data were preprocessed by Statoil. Preprocessing included noise suppression, multiple attenuation, and other standard steps described by Szydlik et al. (2007). Only traces with offsets less than 5 km were kept, and a layer-stripping technique was used to construct a 3D VTI model for prestack depth imaging. The P- and S-wave vertical velocities V_{P0} and V_{S0} and the anisotropy parameters ε and δ in each layer (Figure 15; V_{S0} is not shown) were updated by flattening CIGs (Figure 16a), minimizing misties between seismic and well data, codepthing the key horizons on PP (Figure 16b) and PS migrated sections, and incorporating compressional sonic logs (Szydlik et al., 2007). However, complete information about Statoil's VTI model-building process is not available to us.

Here, we use a 2D section from the 3D P-wave (vertical component) data recorded by the cable laid along $y = 2.8$ km (Figure 14). Two adjacent source lines ($y = 2.8 \pm 0.025$ km) provided 481 shots with a shot interval of 25 m. The tomographic MVA algorithm described above is applied to the CIGs from $x = 2.7$ to 9.5 km with an interval of 50 m, under the assumption that out-of-plane propagation can be ignored. As before, the symmetry axis is assumed to be perpendicular to the interfaces; the parameters V_{P0}, ε, and δ are defined on a 100×50 m grid.

There are two deviated wells (Figure 17a and 17b) in the vicinity of the chosen line, and P-wave reflections are combined in the joint inversion with vertical check-shot (normal-incidence VSP) data recorded in the wells. Although the wells lie outside the vertical plane

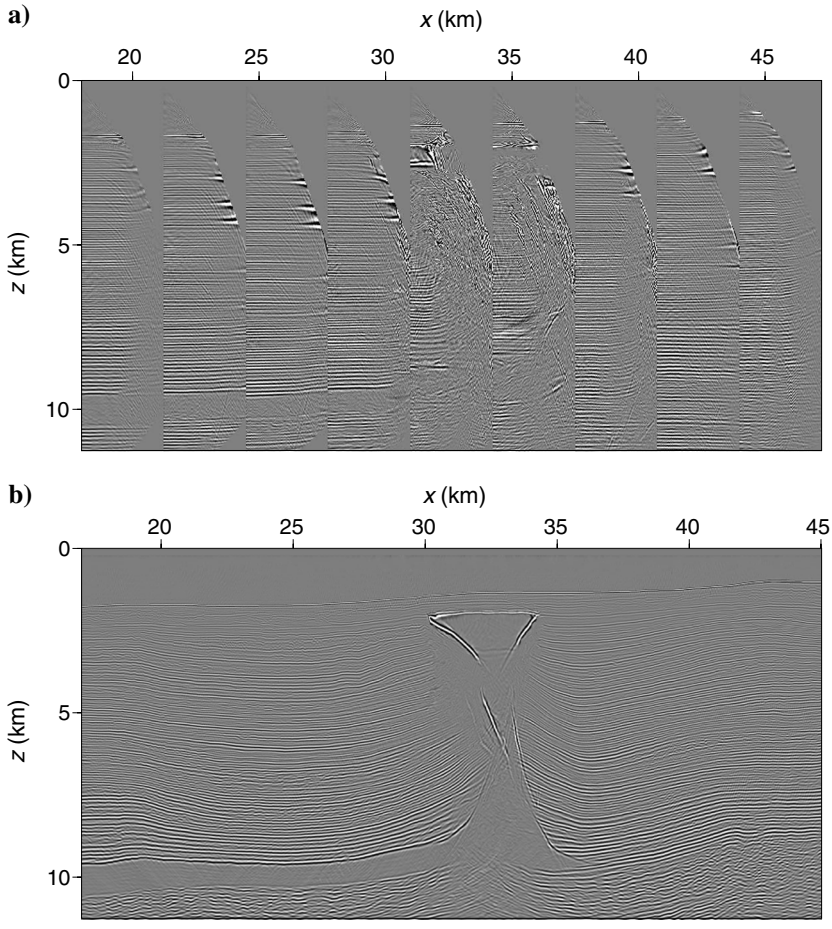

Figure 12. (a) CIGs and (b) the migrated section computed with the final inverted model from Figure 11.

($y = 2.8$ km), only the x (horizontal crossline) and z (vertical) coordinates of the receivers are used to place each check-shot measurement. The provided data set also includes the well markers (i.e., depth measurements in the well) of several key horizons (e.g., the top and base of Utsira formation, top of Shetland Group, and base of Cretaceous). To evaluate the accuracy of velocity analysis, these well markers were compared with the migrated reflector depths (see below).

To build an initial model, the section is divided into eight layers based on key geologic horizons. The interval velocity V_{P0} in each layer is computed from the check-shot traveltimes in well 1, whose surface projection is closer to the chosen line than the projection of well 2 (Figure 17). Assuming the check-shot raypaths and the symmetry axis at the well to be vertical, the velocity is found as $V_{P0} = \Delta z/\Delta t$, where Δz is the depth interval, and Δt is the check-shot traveltime difference corresponding to Δz. The interval NMO velocity (V_{nmo}) and parameter η in each layer are estimated using nonhyperbolic moveout inversion (Tsvankin, 2005) applied to a CMP gather near the well. In combination with the velocity V_{P0} estimated along the well, V_{nmo} and η yield initial guesses for the parameters ε and δ at the well location.

Because of the limited offset-to-depth ratio (smaller than 1.2 for $z > 3$ km), the accuracy of the effective parameters η and ε estimated from nonhyperbolic moveout analysis is insufficient at depth. Also, the interval values of ε and δ may be strongly distorted by layer stripping in the bottom part of the section. Therefore, we have to assume the deeper layers to be isotropic and set ε and δ below

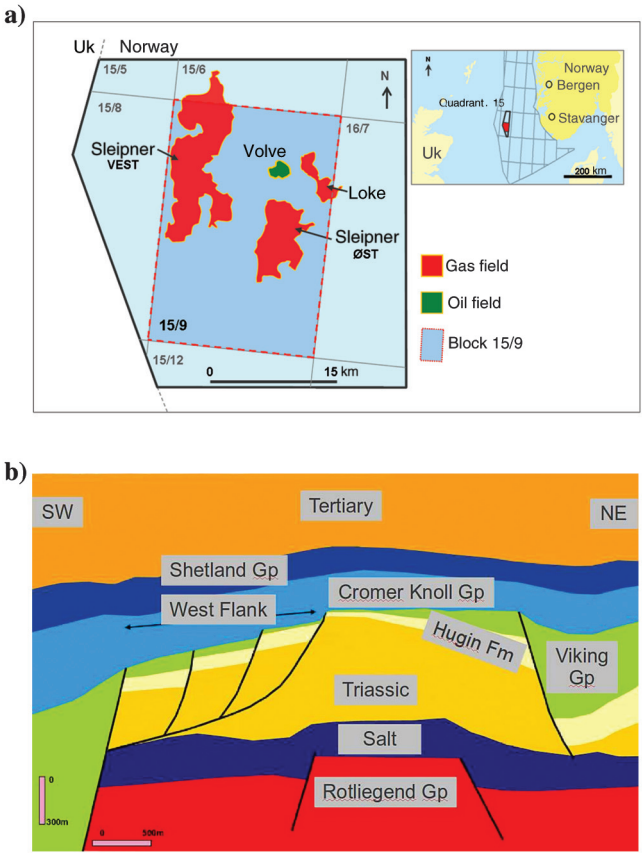

Figure 13. (a) Location of Volve field in the North Sea (figure courtesy of Statoil) and (b) a representative geologic cross-section of Volve field (after Akalin et al., 2010).

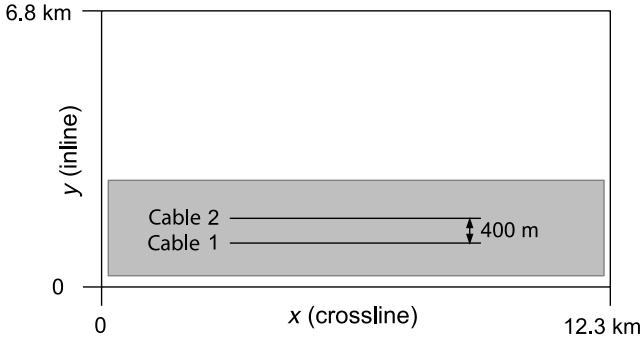

Figure 14. Geometry of the Volve 3D OBS survey. Two cables (black lines) are placed on the seafloor, and 25 sail lines parallel to the cables are shot with flip-flop sources in a 12×2.4 km rectangular area (gray). After one swath of data is recorded, the cables and source lines are moved 800 m along the inline (y) direction.

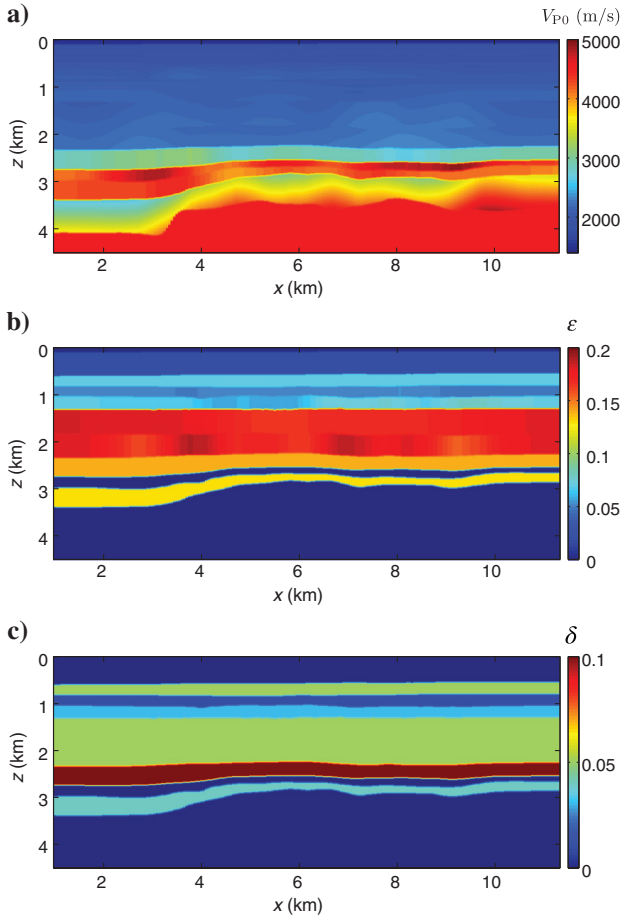

Figure 15. Cross-sections along the line with $y = 2.8$ km (Figure 14) of the 3D VTI model built by Statoil. (a) The P-wave vertical velocity V_{P0} and the anisotropy parameters (b) ε and (c) δ.

3 km to zero (Figure 18b and 18c). The initial TTI model (Figure 18) is obtained by extrapolating the 1D profiles of V_{P0}, ε, and δ at well 1 along the picked interfaces. As expected, the CIGs obtained after Kirchhoff migration with the initial model exhibit noticeable residual moveout (Figure 19).

Using the same three-stage parameter-estimation procedure as in the synthetic tests, we gradually relax the constraints on the spatial variation of ε and δ, while updating V_{P0} at each grid point

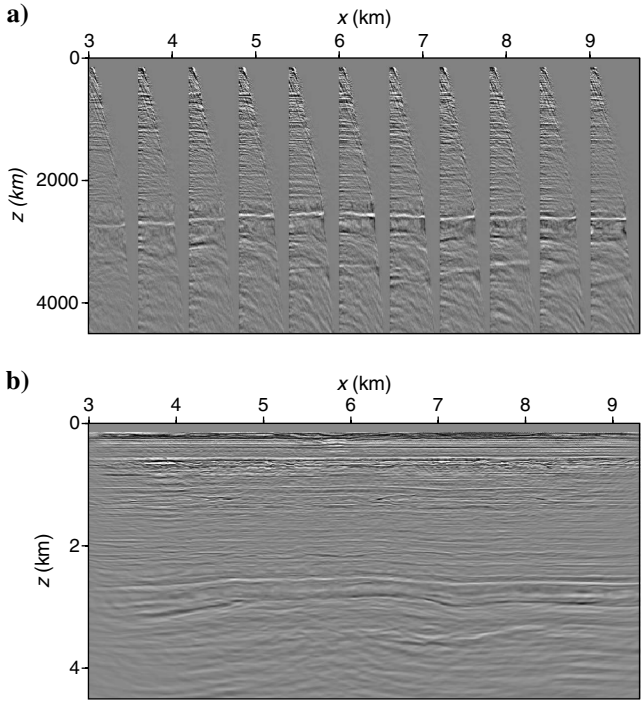

Figure 16. (a) CIGs (displayed every 0.6 km from 3 to 9 km) and (b) the depth image produced by Kirchhoff prestack migration with the parameters from Figure 15.

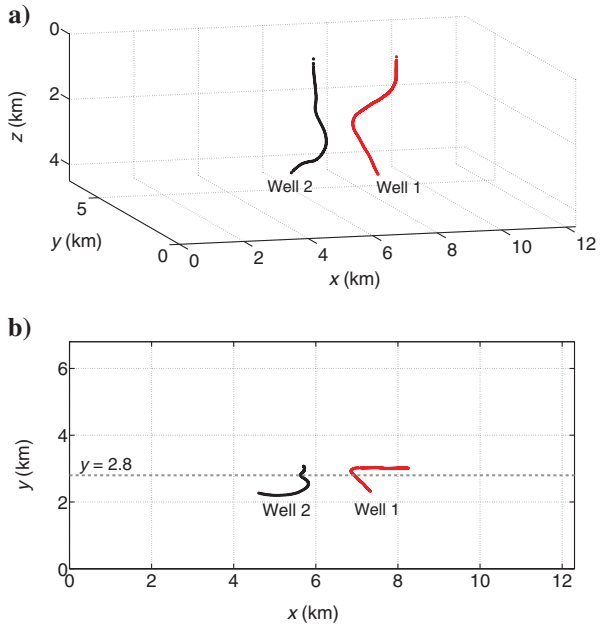

Figure 17. (a) Trajectories of two deviated wells near the line ($y = 2.8$ km, dashed) used for velocity analysis. (b) Well projections onto the horizontal surface. The maximum deviations (Δy) of the two wells from the vertical plane ($y = 2.8$ km) are 477 and 603 m, respectively.

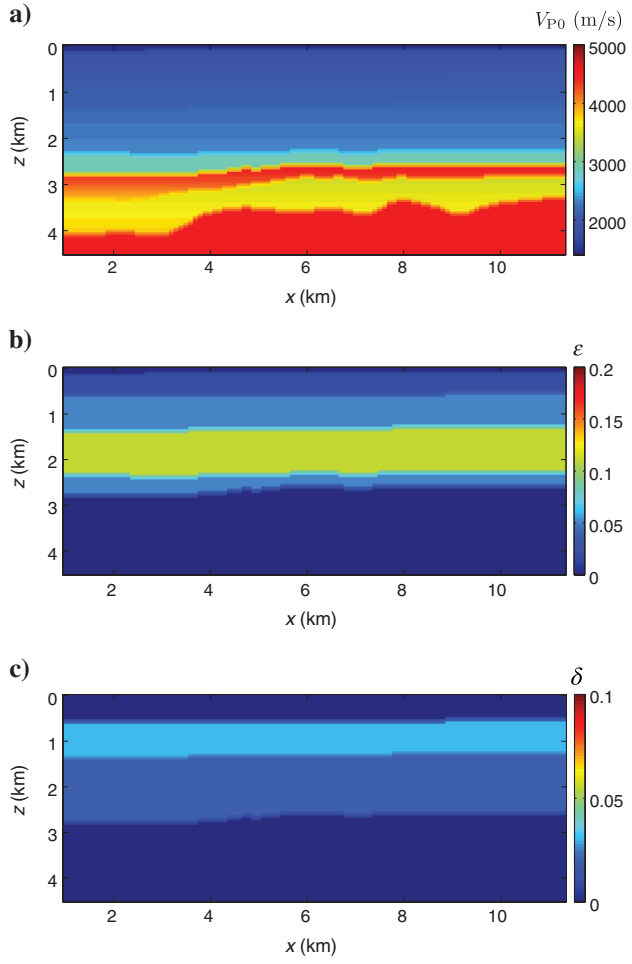

Figure 18. Initial TTI model for line $y = 2.8$ km. (a) The symmetry-direction velocity V_{P0} and the anisotropy parameters (b) ε and (c) δ. All three parameters are defined on a 100×50 m grid.

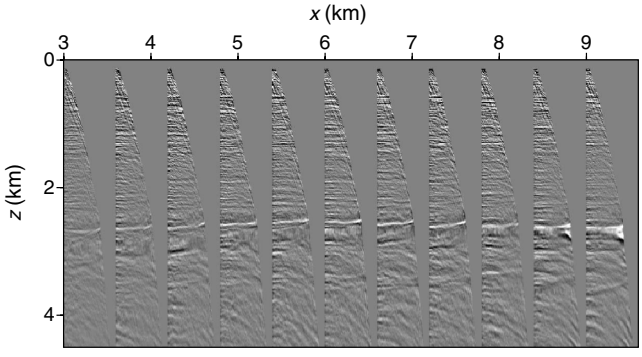

Figure 19. CIGs computed with the initial TTI model from Figure 18.

in all iterations and setting the symmetry axis orthogonal to the reflectors. Each iteration aims to simultaneously minimize the residual moveout in the CIGs and the check-shot traveltime misfit in both wells. In addition, the anisotropic velocity field is regularized by the structure-guided operators defined in equation 2.

The TTI model obtained after 10 iterations of tomography (Figure 20) yields relatively flat CIGs (Figure 21a). The remaining residual moveout in CIGs below $z = 3$ km is partially due to internal multiples that were not completely removed in the preprocessing. As mentioned above, the deeper part of the section ($z > 3$ km) is kept isotropic because of insufficient constraints on the anisotropy parameters provided by reflection data.

The average velocity V_{P0} (Figure 20a) in the Cretaceous Unit (approximately between $z = 2.5$ and 3 km) is reduced after MVA to about 4300 m/s from its initial value 4500 m/s obtained from check shots. In the layer-based VTI model provided by Statoil (Figure 15a), V_{P0} in the Cretaceous Unit is larger, reaching 4900 m/s in some areas. Although the joint tomography used here minimizes the check-shot traveltime misfit in both wells and the structure-guided regularization helps propagate the borehole constraints along the interfaces, the depth scale of the section may not be sufficiently accurate. It is possible that the high velocity in the Cretaceous Unit obtained by Statoil came from sonic logs or other information not available to us.

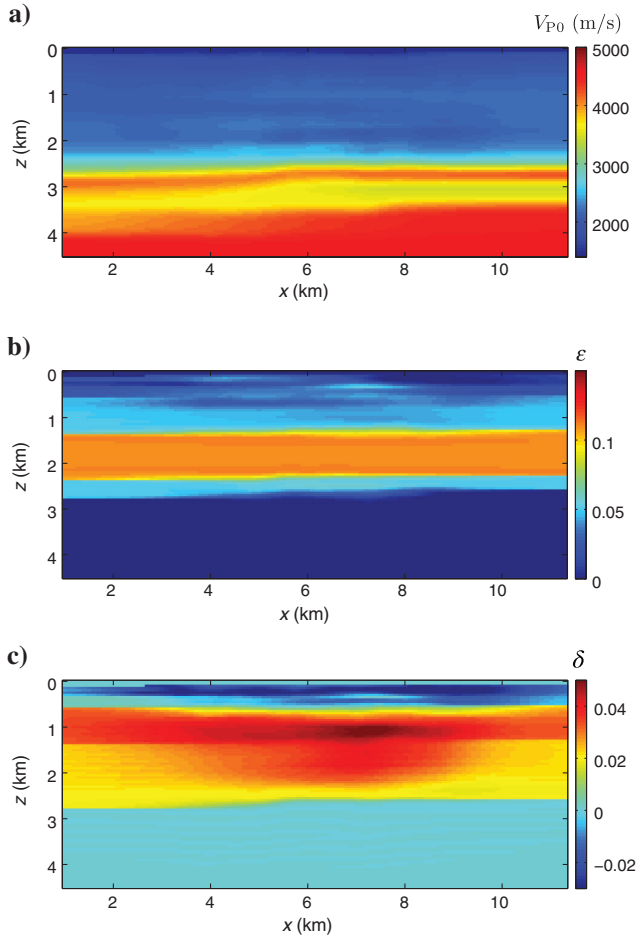

Figure 20. Inverted parameters (a) V_{P0}, (b) ε, and (c) δ after the final iteration of joint tomography.

The inverted model helps image several reflectors in the high-velocity Cretaceous Unit (Figure 22a), which are difficult to identify on the sections computed with the initial model and Statoil's VTI model (Figure 22b). Also, some reflectors beneath the Cretaceous

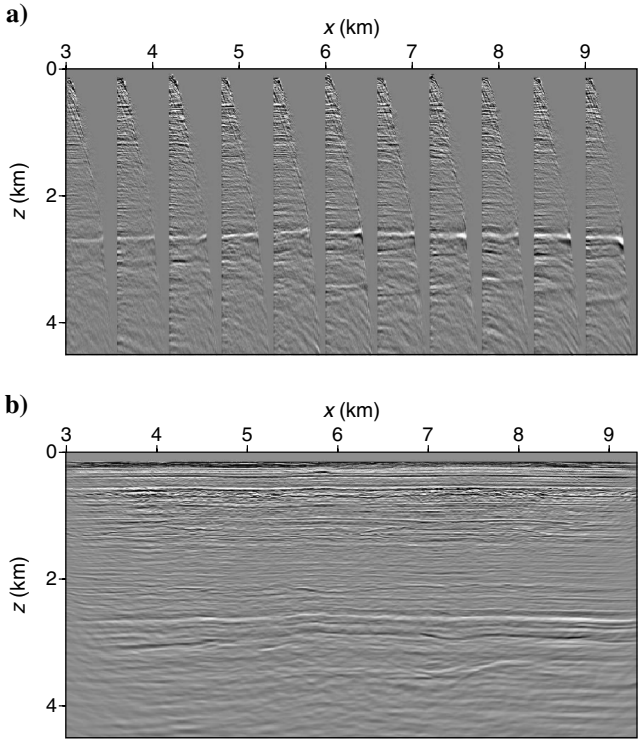

Figure 21. (a) CIGs and (b) the migrated section computed with the final inverted TTI model from Figure 20.

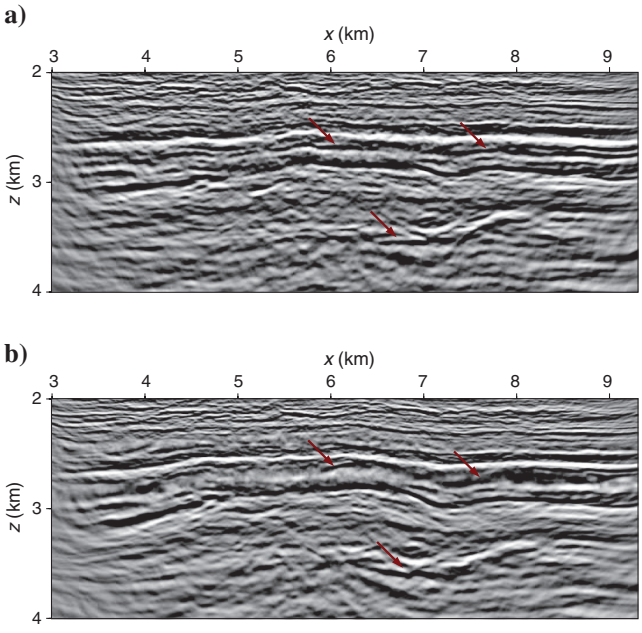

Figure 22. Segment of the migrated section between $z = 2$ and 4 km computed with (a) the inverted model from Figure 20 and (b) the VTI model provided by Statoil (Figure 15).

Unit look more coherent than those imaged with Statoil's model (compare Figure 22a and 22b), which is important for structural interpretation of the reservoir. The key horizons on the final image (Figure 21b) are close to the well markers with the maximum mistie not exceeding 20 m, which confirms that the migrated section has an accurate depth scale near the wells.

There are several possible reasons for the above improvements. One is that the TTI model used here allows the symmetry-axis direction to vary spatially according to the reflector dips. Although the dips are gentle, such a model is more geologically plausible than VTI and should produce more accurate anisotropy parameters. In addition, our joint tomography simultaneously inverts for the TTI parameters defined at all grid points, which helps avoid error accumulation typical for layer stripping.

As any other 2D method, the algorithm applied here is based on the assumption that waves propagate in the vertical incidence plane. However, recorded events may correspond to out-of-plane reflection points; also, the check-shot raypaths in the nearby deviated wells lie outside the incidence plane. Moreover, the symmetry axis, even if it is orthogonal to dipping reflectors, may not be confined to the incidence plane. These 3D phenomena likely explain some remaining residual moveout in CIGs after application of the 2D TTI inversion. To construct a more robust TTI model and make use of the whole OBS data set, our tomographic algorithm should be extended to 3D and, preferably, wide-azimuth data. A major challenge for such 3D tomography, which has to flatten CIGs along different azimuthal directions, is the efficient computation of the Fréchet derivative matrix.

CONCLUSIONS

Although most migration techniques have been extended to TTI media, accurate reconstruction of the anisotropic velocity field remains a difficult problem. Previously, we developed an efficient 2D tomographic algorithm for heterogeneous TTI models, with the parameters V_{P0}, ε, δ, and the symmetry-axis tilt ν defined on a rectangular grid. Whereas V_{P0}, ε, and δ are updated iteratively in the migrated domain, the tilt field is computed from the depth image by setting the symmetry axis perpendicular to the reflectors.

To resolve the TTI parameters in the presence of spatial velocity variations, here we combined reflection data with walkaway VSP and check-shot traveltimes. Our tomographic algorithm also incorporates geologic constraints by appropriately designed regularization. The objective function includes regularization terms that allow for parameter variations across layers, but suppress them in the direction parallel to boundaries. Such structure-guided regularization also helps propagate along interfaces the most reliable parameter updates corresponding to large derivatives in the Fréchet matrix (e.g., those in the cells crossed by dense VSP rays). However, the uncertainty in parameter estimation increases away from the wells, where the anisotropic velocity field is constrained only by reflection data.

To improve the convergence of the algorithm, we proposed a three-stage parameter-updating procedure. In the first several iterations, only the velocity V_{P0} is updated on a grid, while the anisotropy parameters ε and δ are fixed at their initial values. This operation eliminates potentially large distortions in ε and δ caused by the parameter trade-offs. At the second stage of the inversion, ε and δ are taken spatially invariant in each layer and updated together with the grid-based velocity V_{P0}. Finally, all three TTI parameters are estimated simultaneously on the grid with the constraints provided by the regularization terms described above.

First, the joint tomography of reflection and VSP data was tested on two sections of the BP TTI model, one with an anticline and the other with a salt dome. In both tests, a purely isotropic velocity field, which was obtained from check-shot traveltimes and extrapolated along the horizons, served as the initial model. With constraints from P-wave reflection and VSP data, the TTI parameters in the shallow part (above 5 km) of both sections are well resolved. However, the errors in ε and δ increase with depth due to the small offset-to-depth ratio and poor coverage of VSP rays. For the model with the salt dome, the anisotropic velocity field is recovered with higher accuracy to the left of the salt, where the inversion is tightly constrained by VSP data from a nearby well.

The tomographic algorithm was also applied to OBS data from Volve field in the North Sea. Iterative updating of V_{P0}, ε, and δ was performed by joint inversion of P-wave reflection and check-shot data with the structure-guided regularization. An initial anisotropic model was built by combining check-shot traveltimes with nonhyperbolic moveout analysis at the well locations. Then, the three-stage parameter-estimation procedure was used to produce the final gridded TTI velocity field. The inverted TTI model made it possible to focus reflectors within and below the Cretaceous Unit and accurately position several key horizons in depth.

ACKNOWLEDGMENTS

We would like to thank H. Shah of BP for creating the TTI model and BP Exploration Operation Company Limited for generating the synthetic data set (http://www.freeusp.org/2007_BP_Ani_Vel_Benchmark/). We are grateful to Statoil ASA and the Volve license partners ExxonMobil E&P Norway and Bayerngas Norge for the release of the Volve data. The viewpoints about the Volve data set in this paper are of the authors and do not necessarily reflect the views of Statoil ASA and the Volve field license partners. Special thanks to M. Houbiers of Statoil for numerous helpful discussions of the Volve case study. We appreciate constructive reviews of the manuscript provided by I. Vasconcelos, J. Cao, and A. Bakulin. This work was supported by the Consortium Project on Seismic Inverse Methods for Complex Structures at the Center for Wave Phenomena.

REFERENCES

Akalin, A., M. Thompson, J. Mispel, and E. Rundhovde, 2010, Volve — How close communication between the asset team and research was an enabler for field development: PETEX 2010, Expanded Abstracts.

Bakulin, A., Y. Liu, O. Zdraveva, and K. Lyons, 2010a, Anisotropic model building with wells and horizons: Gulf of Mexico case study comparing different approaches: The Leading Edge, **29**, 1450–1460, doi: 10.1190/1.3525359.

Bakulin, A., M. Woodward, D. Nichols, K. Osypov, and O. Zdraveva, 2010b, Building tilted transversely isotropic depth models using localized anisotropic tomography with well information: Geophysics, **75**, no. 4, D27–D36, doi: 10.1190/1.3453416.

Bakulin, A., M. Woodward, O. Zdraveva, and D. Nichols, 2010c, Application of steering filters to localized anisotropic tomography with well data: 80th Annual International Meeting, SEG, Expanded Abstracts, 4286–4290.

Behera, L., and I. Tsvankin, 2009, Migration velocity analysis for tilted TI media: Geophysical Prospecting, **57**, 13–26, doi: 10.1111/j.13652478.2008.00732.x.

Campbell, A., E. Evans, D. Judd, I. Jones, and S. Elam, 2006, Hybrid gridded tomography in the southern North Sea: 76th Annual International Meeting, SEG, Expanded Abstracts, 2538–2541.

Charles, S., D. Mitchell, R. Holt, J. Lin, and J. Mathewson, 2008, Data-driven tomographic velocity analysis in tilted transversely isotropic

media: A 3D case history from the Canadian Foothills: Geophysics, **73**, no. 5, VE261–VE268, doi: 10.1190/1.2952915.
Clapp, R. G., B. L. Biondi, and J. F. Claerbout, 2004, Incorporating geologic information into reflection tomography: Geophysics, **69**, 533–546, doi: 10.1190/1.1707073.
Engl, H. W., M. Hanke, and A. Neubauer, 1996, Regularization of inverse problems: Kluwer Academic Publishers.
Fomel, S., 2007, Shaping regularization in geophysical-estimation problems: Geophysics, **72**, no. 2, R29–R36, doi: 10.1190/1.2433716.
Huang, T., S. Xu, J. Wang, G. Ionescu, and M. Richardson, 2008, The benefit of TTI tomography for dual azimuth data in Gulf of Mexico: 78th Annual International Meeting, SEG, Expanded Abstracts, 222–226.
Morice, S., J.-C. Puech, and S. Leaney, 2004, Well-driven seismic: 3D data processing solutions from wireline logs and borehole seismic data: First Break, **22**, 61–66.
Naumann, U., and O. Schenk, 2011, Combinatorial scientific computing: Chapman & Hall/CRC Computational Science.
Stork, C., 1992, Reflection tomography in the postmigrated domain: Geophysics, **57**, 680–692, doi: 10.1190/1.1443282.
Szydlik, T., P. Smith, S. Way, L. Aamodt, and C. Friedrich, 2007, 3D PP/PS prestack depth migration on the Volve field: First Break, **25**, 43–47.
Tikhonov, A. N., 1963, Solution of incorrectly formulated problems and the regularization method: Soviet Mathematics Doklady, **4**, 1035–1038.
Tsvankin, I., 2005, Seismic signatures and analysis of reflection data in anisotropic media, 2nd ed.: Elsevier Science Publishing Company, Inc.
Wang, X., and I. Tsvankin, 2010, Stacking-velocity inversion with borehole constraints for tilted TI media: Geophysics, **75**, no. 5, D69–D77, doi: 10.1190/1.3481652.
Wang, X., and I. Tsvankin, 2013, Ray-based gridded tomography for tilted transversely isotropic media: Geophysics, **78**, no. 1, C11–C23, doi: 10.1190/geo2012-0066.1.
Woodward, M. J., D. Nichols, O. Zdraveva, P. Whitfield, and T. Johns, 2008, A decade of tomography: Geophysics, **73**, no. 5, VE5–VE11, doi: 10.1190/1.2969907.
Zhou, C., J. Jiao, S. Lin, J. Sherwood, and S. Brandsberg-Dahl, 2011, Multiparameter joint tomography for TTI model building: Geophysics, **76**, no. 5, WB183–WB190, doi: 10.1190/geo2010-0395.1.